International Forum on Aeroelasticity and Structural Dynamics
IFASD 2017
25-28 June 2017 Como, Italy

OPTIMUM DISTRIBUTED WING SHAPING AND CONTROL LOADS FOR HIGHLY FLEXIBLE MISSION-ADAPTIVE AIRCRAFT

Jared R. Hammerton[1], Weihua Su[1], Guoming Zhu[2], Sean Shan-Min Swei[3]

[1]Department of Aerospace Engineering and Mechanics
University of Alabama, Tuscaloosa, AL 35487-0280, United States
suw@eng.ua.edu

[2]Department of Mechanical Engineering
Michigan State University, East Lansing, MI 48824, United States

[3]Intelligent Systems Division
NASA Ames Research Center, Moffett Field, CA 94035, United States

Keywords:

wing shaping control, optimum wing geometry, distributed control, flexible aircraft

Abstract: This paper explores the optimum wing bending and torsion deformations of a highly flexible mission-adaptive aircraft. With the goal of improving flight performance across the entire flight regime, a modal based optimization subject to trim and other constraints is employed. Distributed control loads are formulated and used to determine the optimization wing geometry as well. The optimization is then performed to achieve the best flight performance which is defined as minimum drag. This study explores the optimum wing geometry for steady level flight at a single velocity, a range of velocities, and a coordinated turn. Additionally, the study also explores the optimum wing shapes with the consideration of the trade-off between flight efficiency and ride quality, where a multi-objective optimization is performed, targeting for minimizing drag to improve performance and reducing the wing bending load of a gust to improve the ride quality.

1 INTRODUCTION

The improvement of aircraft operation efficiency needs to be considered over the whole flight plan, instead of a single point in the flight envelope, since the flight condition varies in a flight mission. Therefore, it is natural to employ morphing wing designs so that the aircraft can be made adaptive to different flight conditions and missions. At the advent of recent development in advanced composites as well as sensor and actuator technologies, in-flight adaptive wing/aircraft morphing is now becoming a tangible goal. Traditionally, the discrete control surfaces were used to re-distribute the aerodynamic loads along the wing span during the flight, so as to tailor the aircraft performance. However, the deflection of discrete control surfaces may increase the aerodynamic drag. An effective alternative is to introduce conformal wing/airfoil shape changes for the aerodynamic load control. In addition, the flexibility associated to the morphing wing structures may be pro-actively utilized to improve the aircraft performance. The active aeroelastic tailoring techniques would allow aircraft designers to take advantage of the wing flexibility to create the desired wing load distribution according to the mission requirement, so as to improve overall aircraft operating efficiency and performance, without using the

traditional discrete control surfaces. The utilization of these concepts is predicated upon the optimum shape being known and a control system which is able to produce this wing shape.

The question of determining the optimum wing shape has been studied in depth. Recently, Chen et al. [1] studied the effects of various trim conditions on the aerodynamic shape optimization of the common research model wing-body-tail configuration. Using a free form distribution for the wing geometry coupled with a RANS solver for the aerodynamics their work studied the impact of a trim constraint on the optimization process. Through a series of optimizations utilizing the trim conditions at varying points in the design process, they concluded that considering the trim during optimization yields the best performance. In a similar study, Lyu and Martins [2] performed an aerodynamic optimization of the trailing edge of wing. Their optimization showed that drag reductions could be seen with shape optimization of either the entire wing or just the trailing edge. Taking the optimization a step further requires the development of realistic system capable of producing the optimum shape that is found for a given flight condition. This concept is shown in [3], as the major aspects of the design of the Variable Camber Continuous Trailing Edge Flap (VCCTEF) are highlighted. Along with this detailed design an optimization is performed to determine the deflection angles required throughout the trailing edge to improve the flight performance.

More detailed concepts of wing morphing technologies have been developed as improvements in the materials being used on aircraft and the methods in which they are assembled has improved. In Nguyen et al. [4] the principles of aerodynamic shape optimization and morphing wing structures was explored. The optimization process led into the development of the VCCTEF, which was a novel concept for improving aircraft performance by drag reduction. A further study of the VCCTEF wing model was done by Nguyen and Ting [5], where they performed a flutter analysis of the mission adaptive wing. The methodology included a vortex-lattice aerodynamic model coupled with a finite element structural dynamic model. Urnes et al. [6] provided an updated review of the development, design, and testing of the VCCTEF project. Under the support of the U.S. Air Force Research Laboratory, FlexSys, Inc. developed the Mission Adaptive Compliant Wing (MAC-Wing) to test and evaluate its performance. The adaptive trailing edge flap technology was combined with a natural laminar flow airfoil and tested on the Scaled Composites White Knight aircraft. The testing suggested fuel saving, weight reduction, and improved control authority [7, 8]. In an effort to move from an adaptable trailing edge into a completely adaptable wing structure, the Cellular Composite Active Twist Wing was designed and tested in [9] showing promising results. An airplane model was built, which incorporated two of the active twist wing and was compared to a similar rigid model with traditional control surfaces in wind-tunnel tests. The active twist wing showed similar capabilities for symmetric and asymmetric movements as well as added benefits in stall mitigation. An overview of the process used to design the composite lattice-based cellular structures for active wing shaping was presented in Jenett et al [10]. This paper gave a detailed approach to design a low density, highly complaint structure. The detailed modeling and construction of these structures was also presented.

As optimization processes and morphing technology have improved, there is a need for a complete system, in which a controller will actuate the wing members to the desired optimum shape throughout the entire flight envelope and perform the required maneuver and vibration control during the flight. Most current optimization schemes utilize a CFD aerodynamic model coupled with discrete structural points as design variables. These methods produce promising results, but when considered over an entire flight plan could be a very time consuming process. Addi-

tionally, these methods generally consider the planform shape of the wing rather than the wing bending and torsions associated with highly flexible, large aspect ratio wing members. Recent developments of morphing technologies such as the Cellular Composite Active Twist Wing take advantage of the flexible nature of high aspect ratio wings. Therefore, it is natural to develop an optimization scheme that mainly considers the bending and torsion of the high aspect ratio wings. This concept was utilized in Su et al. [11], which utilized a modal based optimization approach in determining the best feasible wing shape (wing bending and torsion deformations) of a highly flexible aircraft at any given flight scenario. In this paper, this process will be used going forward to develop a wing shape control algorithm with defined distributed control loads. The optimization process will generate the specific wing shape needed to guarantee the optimum performance and ride quality over the entire flight envelope of an aircraft.

2 THEORETICAL FORMULATION

A coupled aeroelastic and flight dynamic formulation for highly flexible aircraft has been developed by Su and Cesnik [12–14]. A brief introduction of the formulation is presented here, followed by the modal-based optimization approach for searching the most efficient wing geometries with the optimum distributed control scheme along the wing span under different flight conditions.

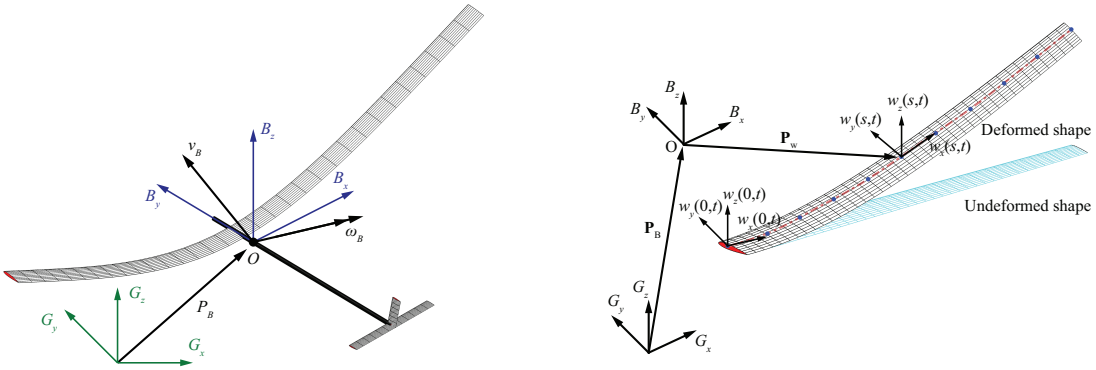

Figure 1: Global and body frames defining the rigid-body motion of aircraft and flexible lifting-surface frames within body frame

2.1 Equations of motion

As shown in Figure 1 a global(inertia) frame G is defined. A body frame $B\,(t)$ is then built in the global frame to describe the vehicle position and orientation. By taking advantage of their geometry, highly flexible wings are modeled as slender beams that may exhibit large deformations in operation. Within the body frame, a local beam frame w is built at each node along the reference line (Figure 1) which is used to define the nodal position and orientation of the flexible members. In Su and Cesnik [15], a nonlinear beam element has been introduced to model the geometrically-nonlinear deformation of slender beams. In this formulation, strain degrees (curvatures) of the beam reference line are considered as the independent variables to describe the beam deformation. Assume the curvatures are constant within one element, the elemental strain vector is denoted as

$$\varepsilon_e^T = \left\{ \begin{array}{cccc} \varepsilon_x & \kappa_x & \kappa_y & \kappa_z \end{array} \right\} \tag{1}$$

where ε_x is the extensional strain, κ_x, κ_y, and κ_z are the twist curvature of the beam reference line, out-of-plane bending curvature, and in-plane bending curvature, respectively. The total

strain vector of the complete aircraft ε is obtained by assembling the global strain vector. Transverse shear strains are not explicitly included in this equation. However, shear strain effects are included in the constitutive relation [16]. Complex geometrically nonlinear deformations can be represented by such a constant-strain distribution over each element.

By following the Principle of Virtual Work extended to dynamic systems, the coupled aeroelastic and flight dynamic behavior of highly flexible aircraft in free flight can be described by the following equations:

$$\begin{aligned}
\mathbf{M}_{FF}(\varepsilon)\ddot{\varepsilon} + \mathbf{M}_{FB}(\varepsilon)\dot{\beta} + \mathbf{C}_{FF}(\dot{\varepsilon},\varepsilon,\beta)\dot{\varepsilon} + \mathbf{C}_{FB}(\dot{\varepsilon},\varepsilon,\beta)\beta + \mathbf{K}_{FF}\varepsilon \\
= \mathbf{R}_F(\ddot{\varepsilon},\dot{\varepsilon},\varepsilon,\dot{\beta},\beta,\lambda,\zeta,\mathbf{T},\mathbf{u}) \\
\mathbf{M}_{BF}(\varepsilon)\ddot{\varepsilon} + \mathbf{M}_{BB}(\varepsilon)\dot{\beta} + \mathbf{C}_{BF}(\dot{\varepsilon},\varepsilon,\beta)\dot{\varepsilon} + \mathbf{C}_{BB}(\dot{\varepsilon},\varepsilon,\beta)\beta \\
= \mathbf{R}_B(\ddot{\varepsilon},\dot{\varepsilon},\varepsilon,\dot{\beta},\beta,\lambda,\zeta,\mathbf{T},\mathbf{u}) \\
\dot{\zeta} = -\frac{1}{2}\Omega_\zeta(\beta)\zeta \\
\dot{\mathbf{P}}_B = \left[\begin{array}{cc} \mathbf{C}^{GB}(\zeta) & \mathbf{0} \end{array}\right]\beta \\
\dot{\lambda} = \mathbf{F}_1\left\{\begin{array}{c} \ddot{\varepsilon} \\ \dot{\beta} \end{array}\right\} + \mathbf{F}_2\left\{\begin{array}{c} \dot{\varepsilon} \\ \beta \end{array}\right\} + \mathbf{F}_3\lambda
\end{aligned} \tag{2}$$

where the components of the generalized inertia $\mathbf{M}$, damping $\mathbf{C}$, and stiffness $\mathbf{K}$ matrices are found in [12, 13]. in general, gravity, aerodynamic loads, thrust, and control forces are considered in the generalized load vector of aircraft, which is given as

$$\begin{aligned}
\left\{\begin{array}{c} \mathbf{R}_F \\ \mathbf{R}_B \end{array}\right\} = \left\{\begin{array}{c} \mathbf{K}_{FF}\varepsilon^0 \\ 0 \end{array}\right\} + \left[\begin{array}{c} \mathbf{J}_{p\varepsilon}^T \\ \mathbf{J}_{pb}^T \end{array}\right]\mathbf{B}^F\mathbf{F}^a + \left[\begin{array}{c} \mathbf{J}_{\theta\varepsilon}^T \\ \mathbf{J}_{\theta b}^T \end{array}\right]\mathbf{B}^M\mathbf{M}^a \\
+ \left[\begin{array}{c} \mathbf{J}_{h\varepsilon}^T \\ \mathbf{J}_{hb}^T \end{array}\right]\mathbf{N}^g\mathbf{g} + \left[\begin{array}{c} \mathbf{J}_{p\varepsilon}^T \\ \mathbf{J}_{pb}^T \end{array}\right]\mathbf{T} + \left[\begin{array}{c} \bar{\mathbf{B}}_F \\ \bar{\mathbf{B}}_B \end{array}\right]\mathbf{u}
\end{aligned} \tag{3}$$

which involves the effects from initial strains ε^0, aerodynamic loads $\mathbf{F}^a$ and $\mathbf{M}^a$, gravitational fields $\mathbf{g}$, thrust force $\mathbf{T}$, and additional control input $\mathbf{u}$. $\mathbf{B}^F$, $\mathbf{B}^M$, and $\mathbf{N}^g$ are the influence matrices for aerodynamic lift, moment, and gravity force, respectively, which come from the numerical integration of virtual work done by the external loads along the wing span (see Su and Cesnik [12]). Influence matrices of the control input ($\bar{\mathbf{B}}_F$ and $\bar{\mathbf{B}}_B$) are dependent on the specific control mechanism and are yet to be determined in this paper. Finally, all the Jacobian matrices $\mathbf{J}$ in Eq. (3) can be obtained from the nonlinear strain-position kinematic relationship discussed in [15, 17], which link the dependent variables (nodal positions and orientations) to the independent variables (element strain and rigid-body motion). It should be noted that both elastic member deformations and rigid-body motions are included when deriving the internal and external virtual work in Su and Cesnik [12]. Therefore, the elastic (ε) and rigid-body (β) degrees of freedom are naturally coupled. This coupling is also highlighted in Eq. (2), where the elastic deformations and the rigid-body motions are solved from the same set of equations.

In Eq. (3), aerodynamics loads are calculated by using the 2-D finite-state inflow theory [18]. At a given station along the wing, the aerodynamics lift, moment, and drag are given as

$$\begin{aligned}
l_{mc} &= \pi\rho_\infty b_c^2\left(-\ddot{z} + \dot{y}\dot{\alpha} - d\ddot{\alpha}\right) + 2\pi\rho_\infty b_c\dot{y}^2\left[-\frac{\dot{z}}{\dot{y}} + \left(\frac{1}{2}b_c - d\right)\frac{\dot{\alpha}}{\dot{y}} - \frac{\lambda_0}{\dot{y}}\right] \\
m_{mc} &= \pi\rho_\infty b_c^2\left(-\frac{1}{8}b_c^2\ddot{\alpha} - \dot{y}\dot{z} - d\dot{y}\dot{\alpha} - \dot{y}\lambda_0\right) \\
d_{mc} &= -2\pi\rho_\infty b_c\left(\dot{z}^2 + d^2\dot{\alpha}^2 + \lambda_0^2 + 2d\dot{z}\dot{\alpha} + 2\dot{z}\lambda_0 + 2d\dot{\alpha}\lambda_0\right)
\end{aligned} \tag{4}$$

where the inflow states λ are governed by the inflow equation in Eq. (2). The different velocity components referred by Eq. (4) can be seen in Figure 2.

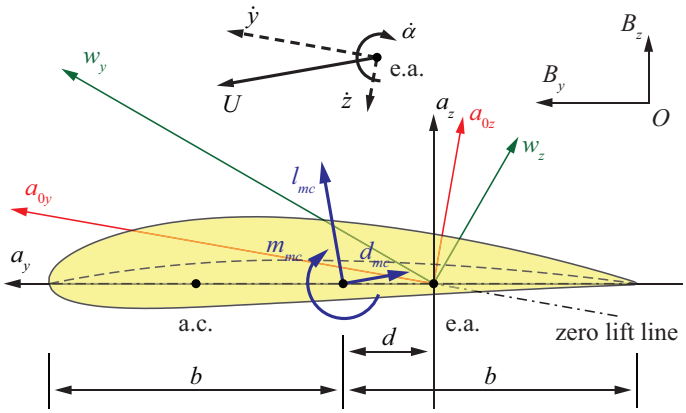

Figure 2: Airfoil coordinate systems and velocity components

2.2 Definition of general distributed control load

In the current study, a distributed control scheme is developed by assuming every element along the main wing can be actuated. Figure 3 shows a generic wing element with applied point force (u_1) and force couplings (ru_2, ru_3 and ru_4) on both ends in order to actuate it. The combined loads may independently actuate the extensive, torsional, out-of-plane bending, and in-plane bending deformations of the element. These elemental loads are written as

$$\begin{aligned}\left(\mathbf{F}_u^{pt}\right)_e &= \left\{ \begin{array}{cccccccccc} -u_1 & 0 & 0 & 0 & 0 & 0 & u_1 & 0 & 0 \end{array} \right\}^T \\ \left(\mathbf{M}_u^{pt}\right)_e &= \left\{ \begin{array}{cccccccccc} -ru_2 & -ru_3 & -ru_4 & 0 & 0 & 0 & ru_2 & ru_3 & ru_4 \end{array} \right\}^T \end{aligned} \tag{5}$$

where the coefficient r represents the arms of force couplings u_1, u_2, and u_3. Without losing generality, r is defined as one in the following studies. Note that there are three nodes defined on each beam element [15]. As no loads are applied at the mid-node of the element for the actuation, the fourth to sixth entries of the load vectors are all zeros. Eq. (5) is further written into the matrix form of

$$\begin{aligned}\left(\mathbf{F}_u^{pt}\right)_e &= \left[\begin{array}{ccccccccc} -1 & 0 & 0 & 0 & 0 & 0 & 1 & 0 & 0 \\ 0 & 0 & 0 & 0 & 0 & 0 & 0 & 0 & 0 \\ 0 & 0 & 0 & 0 & 0 & 0 & 0 & 0 & 0 \\ 0 & 0 & 0 & 0 & 0 & 0 & 0 & 0 & 0 \end{array} \right]^T \left\{ \begin{array}{c} u_1 \\ u_2 \\ u_3 \\ u_4 \end{array} \right\} = \left(\mathbf{B}_u^f\right)_e \mathbf{u}_e \\ \left(\mathbf{M}_u^{pt}\right)_e &= \left[\begin{array}{ccccccccc} 0 & 0 & 0 & 0 & 0 & 0 & 0 & 0 & 0 \\ -1 & 0 & 0 & 0 & 0 & 0 & 1 & 0 & 0 \\ 0 & -1 & 0 & 0 & 0 & 0 & 0 & 1 & 0 \\ 0 & 0 & -1 & 0 & 0 & 0 & 0 & 0 & 1 \end{array} \right]^T \left\{ \begin{array}{c} u_1 \\ u_2 \\ u_3 \\ u_4 \end{array} \right\} = \left(\mathbf{B}_u^m\right)_e \mathbf{u}_e \end{aligned} \tag{6}$$

Accordingly, the complete control loads are obtained by properly sizing and assembling the elemental matrices in Eq. (6), which are

$$\begin{aligned}\mathbf{F}_u^{pt} &= \mathbf{B}_u^f \mathbf{u} \\ \mathbf{M}_u^{pt} &= \mathbf{B}_u^m \mathbf{u} \end{aligned} \tag{7}$$

where $\mathbf{F}_u^{pt}$ and $\mathbf{M}_u^{pt}$, as point loads, can be eventually transformed to the generalized control load by using the Jacobians:

$$\begin{aligned}\left\{ \begin{array}{c} \mathbf{R}_F^u \\ \mathbf{R}_B^u \end{array} \right\} &= \left[\begin{array}{c} \mathbf{J}_{p\varepsilon}^T \\ \mathbf{J}_{pb}^T \end{array} \right] \mathbf{F}_u^{pt} + \left[\begin{array}{c} \mathbf{J}_{\theta\varepsilon}^T \\ \mathbf{J}_{\theta b}^T \end{array} \right] \mathbf{M}_u^{pt} \\ &= \left(\left[\begin{array}{c} \mathbf{J}_{p\varepsilon}^T \\ \mathbf{J}_{pb}^T \end{array} \right] \mathbf{B}_u^f + \left[\begin{array}{c} \mathbf{J}_{\theta\varepsilon}^T \\ \mathbf{J}_{\theta b}^T \end{array} \right] \mathbf{B}_u^m \right) \mathbf{u} = \left[\begin{array}{c} \bar{\mathbf{B}}_F \\ \bar{\mathbf{B}}_B \end{array} \right] \mathbf{u} \end{aligned} \tag{8}$$

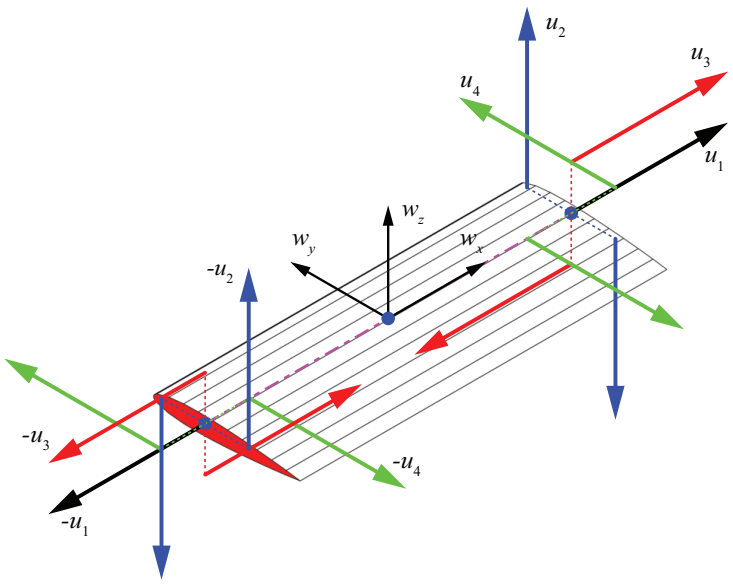

Figure 3: Point control forces on a beam element (Black: extension force; Blue: torsion coupling; Red: out-of-plane bending coupling; and Green: in-plane bending coupling).

2.3 Determination of optimum wing geometry

Under a given flight condition (U_∞ and ρ), the optimum wing geometry and other control inputs should be determined to satisfy the trim of aircraft. In general, the trim variables are:

$$q_{trim} = \left\{ \begin{array}{cccc} \alpha_B & \varphi_B & \mathbf{T} & \mathbf{u} \end{array} \right\}^T \tag{9}$$

where α_B is the body pitching angle, φ_B is the bank angle, and $\mathbf{u}$ is the control input as defined in Sec. 2.2. With the rigid-body rotation angles, one can prescribe the quaternions and rigid-body velocity:

$$\begin{aligned} \zeta &= \zeta(\alpha_B, \varphi_B) \\ \beta &= \beta(U_\infty, \zeta) \end{aligned} \tag{10}$$

Therefore, the original aeroelastic and flight dynamic equations (Eq. 2) are reduced to steady-state equilibrium equations, after removing the transient terms and unsteady aerodynamic contributions, which are

$$\begin{aligned} \mathbf{K}_{FF}\varepsilon - \mathbf{R}_F(\alpha_B, \varphi_B, \mathbf{T}, \mathbf{u}, \varepsilon) &= \mathbf{0} \\ \mathbf{R}_B(\alpha_B, \varphi_B, \mathbf{T}, \mathbf{u}, \varepsilon) &= \mathbf{0} \end{aligned} \tag{11}$$

where the loads are explicitly determined by the trim variables, as well as the wing shape. It is clear that the second entry of Eq. (11) is essentially the trim condition that an aircraft in steady flight should satisfy, while the first is the elastic equilibrium only for flexible aircraft.

In the study of Su et al. [11], a modal-based approach was developed to search for the optimum wing geometry without using the traditional control surfaces. This approach is still utilized here, where the wing geometry is represented by linear mode shapes, such that

$$\bar{\varepsilon}(s,t) = \sum_{i=1}^{N} \Phi_i(s)\eta_i(t) \tag{12}$$

where Φ are the linear mode shapes of the flexible aircraft and η are the corresponding magnitudes of the modes. This approach allows one to use a finite number of modes to search for the optimum wing shape, targeting for the minimum drag as the optimum flight performance, while maintaining the trim and elastic equilibrium of the aircraft.

$$\begin{aligned} \mathbf{r}_F &= \mathbf{K}_{FF}\bar{\varepsilon} - \mathbf{R}_F(\alpha_B, \varphi_B, \mathbf{T}, \mathbf{u}, \eta_1, \eta_2, \cdots, \eta_N) \\ \mathbf{r}_B &= \mathbf{R}_B(\alpha_B, \varphi_B, \mathbf{T}, \mathbf{u}, \eta_1, \eta_2, \cdots, \eta_N) \end{aligned} \tag{13}$$

From Eq. (13) and Eq. (8) the control force $\mathbf{u}$ can be calculated during each step of the optimization process as

$$\mathbf{u} = \bar{\mathbf{B}}_F^{-1}\left(\mathbf{K}_{FF}\bar{\varepsilon} - \mathbf{J}_{p\varepsilon}^T\mathbf{B}^F\mathbf{F}^a - \mathbf{J}_{\theta\varepsilon}^T\mathbf{B}^M\mathbf{M}^a - \mathbf{J}_{h\varepsilon}^T\mathbf{N}^g\mathbf{g} - \mathbf{J}_{p\varepsilon}^T\mathbf{T}\right) \tag{14}$$

With the elastic equilibrium now satisfied, the optimization problem is defined as

$$\begin{aligned} &\min_q D = D(q) \\ &s.t. \quad \mathbf{r}_B = 0 \\ &q = \left\{ \begin{array}{ccccccc} \alpha_B & \varphi_B & \mathbf{T} & \eta_1 & \eta_2 & \cdots & \eta_N \end{array} \right\}^T \end{aligned} \tag{15}$$

2.4 Multi-objective function optimization

It may be desired to determine a shape which accomplishes a goal other than minimizing drag. Highly-flexible aircraft with slender wings are often susceptible to the effects of a gust. To account for this, another objective function is required so as to minimize the wing bending moment due to gust disturbances. This function will then be combined with the minimum drag objective to formulate a multi-objective optimization problem. This allows for a study to be performed to understand the various shapes required to find the trade-off between the minimum drag and the minimum gust effects.

A discrete gust model is used to calculate the moment a gust could generate on root of the wing. The desired gust model is shown in Figure 4. The gust should have a width 25 times longer than the chord of the wing, which for this particular study would result in a gust that is 25 meters long. The gust velocity can be expressed as here

$$w_{gust} = \frac{w_0}{2}\left(1 - cos\left(\frac{2\pi x}{25c}\right)\right) \tag{16}$$

To further simplify the problem a method similar to [19] will be used. This reduces the gust so that the entire streamwise length of the airfoil section experiences the same value of the gust velocity at a given time. This gives an effective angle of attack as expressed here

$$\alpha_g = \frac{1}{2}\frac{w_0}{U_0}\left(1 - cos\left(\frac{2\pi x}{25c}\right)\right) \tag{17}$$

The maximum angle of attack will occur as

$$(\alpha_g)_{max} = \frac{w_0}{U_0} \tag{18}$$

from which the resulting aerodynamic loads can be calculated.

The alleviation of the gust load can be approximated by minimizing the induced bending moment M_y at the root of the wing. Using this along with the aerodynamic drag calculation used in the single objective function optimization the new objective function can be defined as

$$f_{obj} = \xi D + (1 - \xi) M_y \tag{19}$$

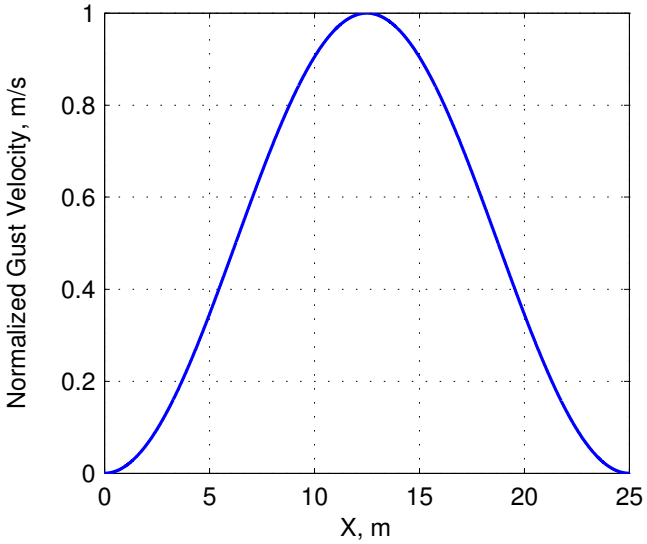

Figure 4: 1-cosine gust model velocity profile

3 NUMERICAL RESULTS

In this section, a highly flexible aircraft model is considered for the numerical study. The vehicle's geometrical and physical properties are shown in Figure 5 and Table 1. The aircraft has a wingspan of 32 m and a total mass of 54.5 kg.

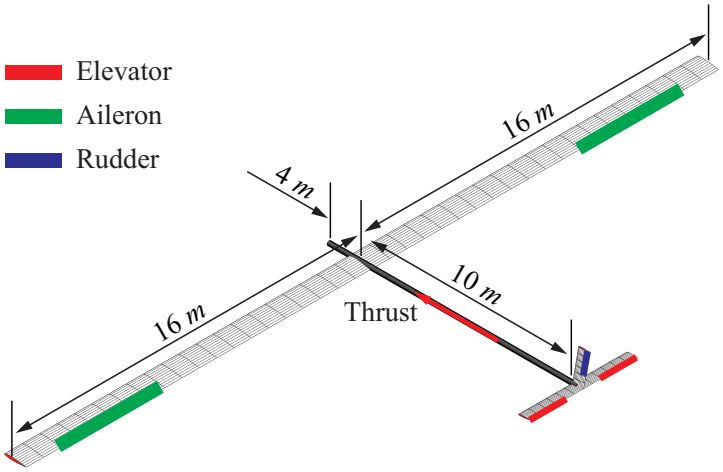

Figure 5: Geometrical data of the baseline highly flexible aircraft

Parameter	Value	Unit
Wings		
Span	16	m
Chord	1	m
Incidence angle	2	deg
Sweep angle	0	deg
Dihedral angle	0	deg
Beam reference axis (from LE)	50	% chord
Cross-sectional c.g. (from LE)	50	% chord
Mass per span	0.75	kg·m
Rotational moment of inertia	0.1	kg·m
Torsional rigidity	1.00×10^4	N·m^2
Flat bending rigidity	2.00×10^4	N·m^2
Edge bending rigidity	4.00×10^6	N·m^2
Tails		
Span of horizontal tail	2.5	m
Span of vertical tail	1.6	m
Chord of tails	0.5	m
Incidence of horizontal tail	-3	deg
Incidence of vertical tail	0	deg
Sweep of horizontal tail	10	deg
Dihedral of horizontal tail	0	deg
Beam reference axis (from LE)	50	% chord
Cross-sectional c.g. (from LE)	50	% chord
Mass per span	0.8	kg·m
Rotational moment of inertia	0.01	kg·m
Torsional rigidity	1.00×10^4	N·m^2
Flat bending rigidity	2.00×10^4	N·m^2
Edge bending rigidity	4.00×10^6	N·m^2
Complete aircraft		
Mass	54.5	kg

Table 1: Properties of the baseline highly flexible aircraft

3.1 Steady Level Flight

In this study, the altitude of steady level flight is kept constant at 20,000 m and the flight speed is fixed as 25 m/s. An optimization similar to what was performed in [11], updated to include the distributed control force calculation as described above, is used to determine the optimum wing shape. The optimization utilizes the trim conditions of the conventional aircraft configuration with discrete control surfaces (see Figure 5) as the initial condition, and then explores the design space by changing the body pitch angle, thrust, and modal magnitudes to minimize the drag while maintaining trim. For this optimization process, the first seven symmetric modes are used as design variables, as steady level flight produces symmetric wing deformations [11]. The resulting optimum shape for the steady level flight case can be seen in Figure 6. The resulting shape is primarily composed of the first and third bending modes. A deep "U" shape from the root is produced by the first mode, and the third (second symmetric) mode produces a downward bending of the wing tips. The optimum shape is compared to the initial trim case in Table 2.

This shows the drag reduction of approximately 12.7% between the initial and optimum shapes.

	Initial	Optimum
Body pitch angle, deg	1.2596	2.8856
Thrust, N	59.2823	51.7633
Mode 1	1.5654	0.6697
Mode 3	-0.0164	-0.1555
Mode 5	0.0071	-0.0004
Mode 7	0.0004	-0.0008
Mode 8	0.0005	0.0135
Mode 10	-0.0002	0
Mode 12	-0.0014	-0.0005
Drag, N	59.84	51.696

Table 2: Initial and optimum wing shape for U = 25 m/s.

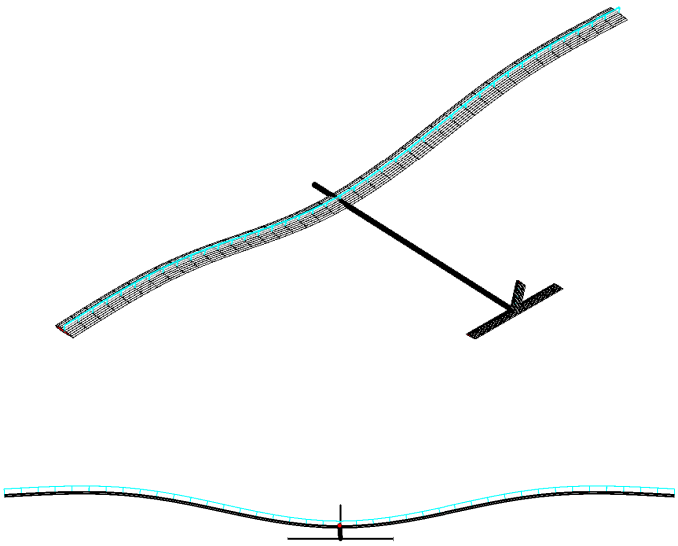

Figure 6: Optimum wing shape for steady level flight at 25 m/s

The full distributed control force **u** is plotted in Figure 7. The four curves shown are the Extension force, the torque, the out-of-plane bending moment, and the in-plane bending moment for each element of the right wing. Since the steady level flight results in a symmetric wing deformation, the control force in the left wing is simply a mirror to the right. It can be seen that the distributed force is dominated by the out-of-plane bending moment, which agrees with the shape seen in Figure 6.

3.2 Level Flight Velocity Range: 18 - 28 m/s

An aircraft may experience a wide variety of flight conditions over the course of their flight plane. This will require separate optimum shapes for each different flight condition experienced. This section explores the various optimum wing geometries associated with varying flight velocities that the aircraft might encounter. Specifically, the range of 18 to 28 m/s is explored. Each of these cases is treated as an individual steady level flight case, meaning again only the symmetric modes are considered as design variables. The aircraft model is again trimmed using the traditional control surfaces for each flight velocity in order to have a point

of comparison with the optimum solution as well as an initial set of design variables. Some of the trim results are expressed in Table 3 for both the initial and optimum cases. One measure in the effectiveness of the optimization is to examine the percent difference in the thrust required. This gives an idea into the potential energy savings of the optimum wing shape versus the initial wing shape. For this velocity range the varying percent difference is as great as 12.68% and as low as 4.64% meaning the drag reduction is somewhat dependent on the specific flight condition.

	Initial			Optimum		
U, m/s	Drag, N	Thrust, N	BAOA, deg	Drag, N	Thrust, N	BAOA, deg
18	105.254	105.974	6.595	100.799	101.061	4.1077
19	95.571	96.011	5.485	90.278	90.468	3.721
20	87.195	87.468	4.528	82.724	82.864	3.353
21	79.943	80.110	3.699	77.479	73.586	3.210
22	73.657	73.756	2.973	66.992	67.085	3.041
23	68.190	68.245	2.333	61.091	61.177	2.940
24	63.424	63.454	1.766	56.053	56.121	2.906
25	59.268	59.282	1.260	51.696	51.763	2.886
26	55.659	55.665	0.803	50.246	50.325	3.140
27	52.520	52.521	0.389	49.733	49.806	3.078
28	49.811	49.811	0.010	41.287	45.604	2.463

Table 3: Initial and optimum trim data for U = 18 to 28 m/s

Table 4 lists the magnitudes of the modes that describe the shapes of the resulting optimum wing geometries. Figures 8 to 11 highlight four distinct shapes seen over the velocity range. The shapes from U = 18 m/s to U = 24 m/s are all similar, which is bent upward at the root and then begins to flatten out towards the wing tip. The optimum shape at U = 25 m/s begins the transition from the flatter shape into a deep"U" shape. The shape at U = 26 m/s begins to show the deep "U", while still having the wing tips bend down towards flat. Finally, at U = 28 m/s, the full deep "U" shape is reached. This trend is also present in the modal magnitudes as

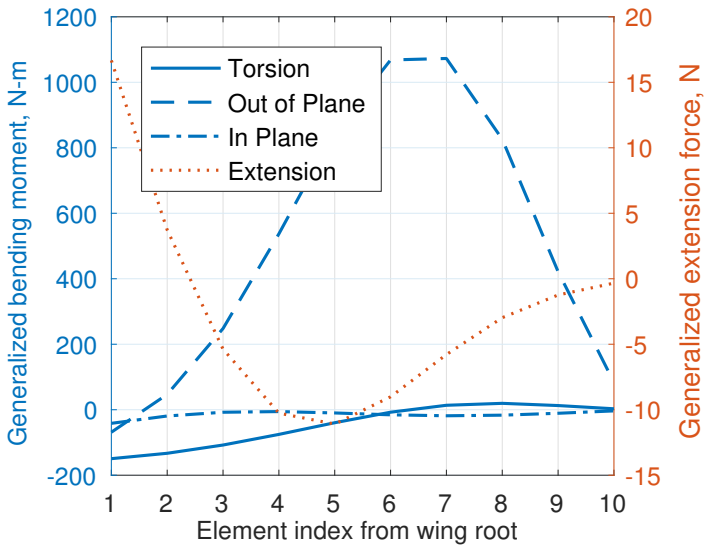

Figure 7: Distributed control force of the optimum wing shape

flight velocities over 26 m/s have significantly larger magnitudes for Mode 1, which results in the "U" shape. It is important that the shapes for the varying flight conditions are similar, so that in future work when a controller is designed, the transitions of controllers between flight conditions are reasonable and possible. This is visibly true as the shapes gradually shift from the flatter shape to the deep "U" shape. The magnitudes of Modes 1 and 3 also demonstrate this to some extent, as the magnitude of Mode 1 generally increases as the velocity increases and the magnitude of Mode 3 generally decreases as the velocity increases.

U, m/s	Mode 1	Mode 3	Mode 5	Mode 7	Mode 8	Mode 10	Mode 12
18	0.6771	-0.1476	-0.0104	-0.0011	-0.0015	-0.0005	-0.0091
19	0.6621	-0.1541	-0.0086	-0.0009	-0.0015	-0.0004	-0.0074
20	0.4619	-0.0353	-0.0073	0.0139	0.0372	0.0132	0.0001
21	0.4993	-0.1460	-0.0052	0.0071	0.0090	0.0068	-0.0061
22	0.5537	-0.1531	-0.0041	-0.0025	0.0069	-0.0003	-0.0043
23	0.5122	-0.1616	-0.0030	-0.0015	0.0007	-0.0003	-0.0034
24	0.5643	-0.1629	-0.0017	-0.0011	-0.0046	-0.0003	-0.002
25	0.6697	-0.1555	-0.0004	-0.0008	0.0135	0.0000	-0.0005
26	1.3127	-0.0958	-0.0001	-0.0006	0.0045	0.0001	0.0017
27	1.4958	0.0616	-0.0009	-0.0007	-0.0008	-0.0003	-0.0008
28	1.5906	-0.0406	0.0006	-0.0011	-0.0006	-0.0003	0.0007

Table 4: Modal Magnitudes for Optimum Shapes for U = 18 to 28 m/s

The full distributed force for a few highlighted cases are presented in Figures 12 to 15. It can be seen again that the distributed control force is dominated by the out-of-plane bending. At the higher velocities the torsional component becomes more prominent as well.

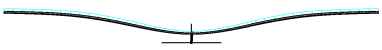

Figure 8: U = 18 m/s

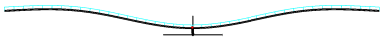

Figure 9: U = 25 m/s

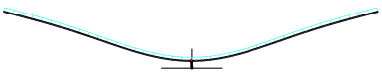

Figure 10: U = 26 m/s

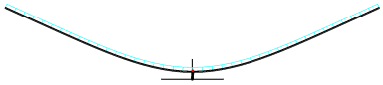

Figure 11: U = 28 m/s

3.3 Steady Coordinated Turn

Optimum wing geometry for steady coordinated turning flight is also explored. Maintaining the 20,000 m altitude, the aircraft is subjected to a 20.50 m/s nominal turn speed, which is chosen to produce wing tip deflection similar to that of the 25 m/s steady level flight case. This adds additional constraints into the optimization process and adds the aircraft bank angle as a design variable, which is constrained up to 35 degrees. The trim values and modal magnitudes for the initial and optimum cases are presented in Table 5. It can be seen that the optimum geometry has a drag reduction of 8.9% which is comparable with the reductions seen in the steady level

flight case.

	Initial condition	Optimum solution
Body pitch angle, deg	4.44	3.58
Bank angle, deg	14.97	17.12
Thrust, N	92.19	83.92
Mode 1	1.5529	0.6780
Mode 2	-0.0069	-0.0219
Mode 3	-0.0182	-0.1479
Mode 4	0.0000	0.0000
Mode 5	0.0074	-0.0062
Mode 6	0.0022	0.0004
Mode 7	0.0006	0.0075
Mode 8	0.0007	0.0145
Mode 9	0.0011	-0.0112
Mode 10	-0.0002	-0.0002
Mode 11	0.0000	-0.0002
Mode 12	-0.0017	-0.0050
Drag, N	91.92	83.76

Table 5: Optimum wing shape for steady coordinated turn

The optimum wing geometry is shown in Figure 16. It is of note that the shape of the steady coordinated turn is very similar to the shape of the 25 m/s level flight case. The dominate modes in each case are the first and third modes and the magnitudes are very similar between the two

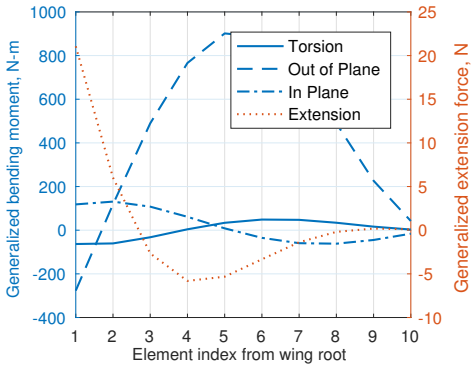

Figure 12: Distributed control force U = 18 m/s

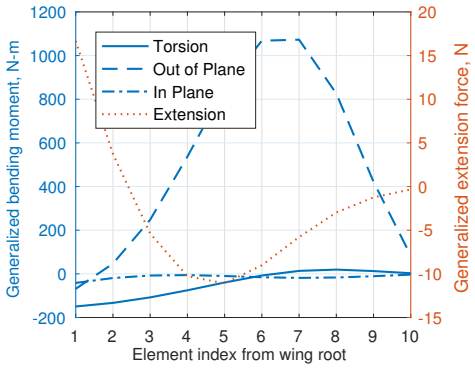

Figure 13: Distributed control force U = 25 m/s

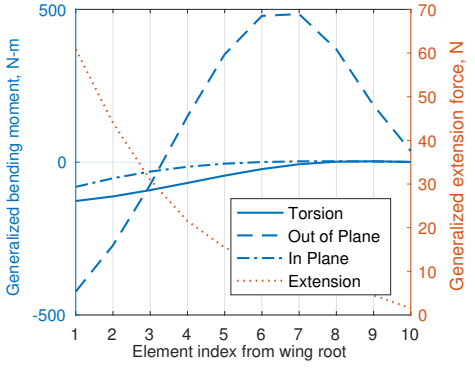

Figure 14: Distributed control force U = 26 m/s

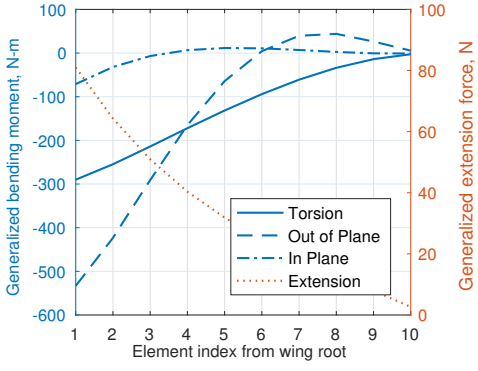

Figure 15: Distributed control force U = 28 m/s

cases. The antisymmetric modes are also a factor in this new shape because of the turning maneuver.

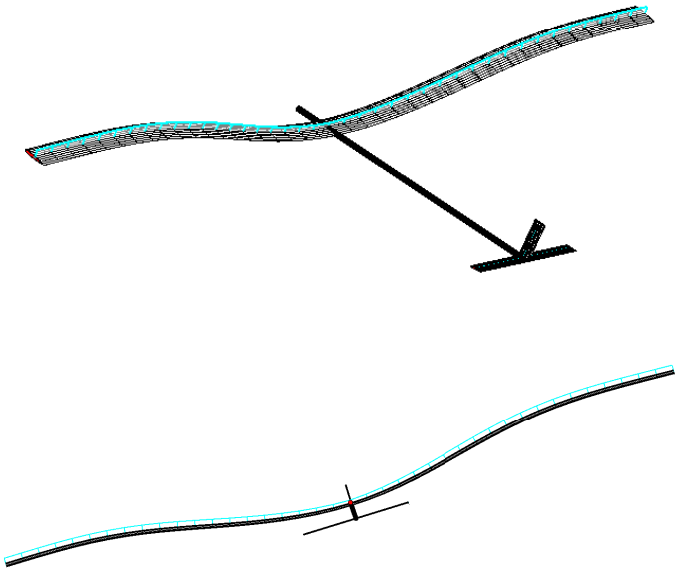

Figure 16: Optimum wing shape for steady coordinated turn

3.4 Multi-objective Optimization

Using the updated multi-objective function in Equation 19, a new optimization is performed to study the effects of varying the parameter ξ. For this study, the aircraft is again at 20,000 m and flying at 25 m/s. Only the symmetric modes are used in the optimization as it is still steady level flight. The parameter ξ is varied from 0 to 1 in increments of 0.1. If ξ=1 the optimization is solely to minimize the drag, and if ξ = 0 the optimization is solely to minimize the wing root bending moment due to gust disturbances. The results of this study are shown in Table 6 including the aerodynamic drag, thrust, body angle of attack for trim, and the root bending load for each case. It can be seen that as ξ goes from 0 to 1, the drag from the final solution decreases, until it reaches the same solution that was achieved in the single objective function optimization. The bending moment at the root of the wing follows an opposite pattern, increasing as ξ increases. These two patterns demonstrate the trade-off that is associated with the objective function. This study provides insight into methods, in which aircraft designers could build a control system. If an aircraft is known to experience gusts often, the optimum shape would be one which considers the minimum moment at the wing root more heavily than the minimum drag.

The optimum shapes associated with a few highlighted cases are presented in Figures 17 to 20. The chosen velocities represent the major shapes seen as ξ is varied. Low values of ξ have a shape similar to Figure 17, which is flat at the root and then bends upward at the wing tip. A ξ increases the shape shifts to something similar to Figure 18 which is more of a deep "U" shape with the wing tips starting to show signs of bending down. As ξ is further increased, the shape again bends upward at the root but then begins to flatten out at the wing tip. Finally as xi approaches 1, the shape becomes the shape that was obtained in the steady level flight single objective function optimization, where the root bends upward and then around halfway through the span, the wing begins to bend back down until the shape is nearly flat.

ξ	Drag(N)	Thrust(N)	Body AOA(deg)	M_y(N-m)
0	-81.88	82.09	4.16	1.9741×10^3
0.1	-82.19	82.35	3.59	1.9353×10^3
0.2	-81.9	82.15	4.56	1.9916×10^3
0.3	-70.63	70.79	3.95	2.2221×10^3
0.4	-63.93	64.09	4.09	2.4949×10^3
0.5	-58.63	58.74	3.68	2.6965×10^3
0.6	-56.49	56.61	3.49	2.8343×10^3
0.7	-56.39	56.49	3.47	2.8492×10^3
0.8	-54.11	54.19	3.23	3.0317×10^3
0.9	-53.39	53.46	3.10	3.161×10^3
1	-51.66	51.72	2.87	3.1436×10^3

Table 6: Parametric Study Results

Included in Figure 21 is a plot of the root bending moment vs drag for values of ξ ranging from 0 to 1. This plot serves as a tool for potential aircraft designers to understand the relationship between performance and ride quality in the optimization process. There is a clear trade-off, as well as what appears to be a range of values in the middle that offer improvement in both performance and ride quality.

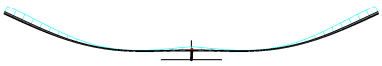

Figure 17: ξ=0

Figure 18: ξ=0.4

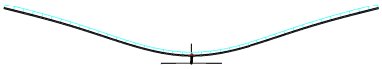

Figure 19: ξ=0.8

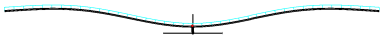

Figure 20: ξ=1

4 CONCLUSIONS

Determination of the optimum wing geometry of a highly flexible aircraft under varying flight conditions was explored in this paper. Given the flexible nature of high aspect ratio aircraft, a modal based approach was used in determining the optimum wing bending and torsion geometry. The magnitudes of the modes were used as design variables within the optimization. Additionally, a distributed control actuation was formulated by assuming each element of the main wing could be actuated. This gave an insight into the forces and moments required to generate a specific wing geometry. The distributed force calculation was included within the optimization and it was verified using a steady level flight case.

Additionally, the optimization was expanded to a range of velocities better understand the optimum wing shape and the required control actuation with variable flight conditions. A smooth

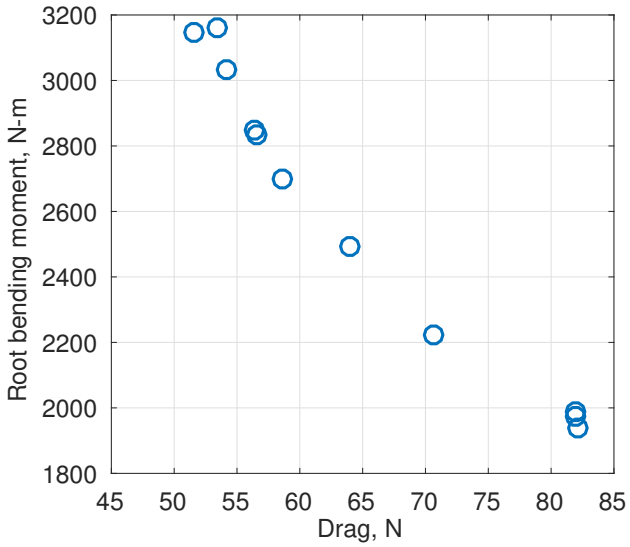

Figure 21: Root bending moment versus drag for ξ = 0-1

transition of optimum geometries was seen. As the velocities became higher, the first mode became dominate and the third mode became less important. The optimization was also applied to a steady coordinated turn maneuver. This required the presence of the antisymmetric modes in the optimization. The resulting geometry from the turning maneuver was similar to that of the steady level flight. Finally, the optimization was updated to include gust alleviation as an objective function. This multi-objective function provided insights into the trade-off between performance metrics minimum drag and best riding quality.

It should be noted that the optimization was computed using the gradient-based optimizer *fmincon* in MATLAB, which can only produce a local minimum. Despite not being a global minimum, the results produced were consistent and showed significant improvement over the baseline solution. The results presented here serve as the foundation of future works to develop the robust flight control algorithms to determine the optimum wing geometry for any flight condition. It has been demonstrated that the optimum shape over a range of velocities follows what appears to be a visually smooth transition. These results will be used along with linear parameter-varying modeling techniques to develop a flight controller. A similar process will also be used with the coordinated turn results, to demonstrate the effects of the optimum shape on a turning maneuver. Currently, the objective function is to minimize the drag experienced by the aircraft. However, it is also of importance to consider minimizing the control effort needed to maintain a particular wing geometry. Going forward, additional multi-objective optimizations will be performed, to find a desirable balance between the various design needs of the aircraft.

5 ACKNOWLEDGMENT

The research is supported by the Convergent Aeronautics Solutions (CAS) project of NASA ARMD. The first author also acknowledges the support of the Alabama Space Grant Consortium (ASGC) Fellowship. The views expressed in this paper are those of the authors and do not reflect the official policy or position of NASA or the U.S. Government.

6 REFERENCES

[1] Chen, S., Lyu, Z., Kenway, G. K. W., et al. (2016). Aerodynamic Shape Optimization of Common Research Model WingBodyTail Configuration. *Journal of Aircraft*, 53(1), 276–293. ISSN 0021-8669. doi:10.2514/1.C033328.

[2] Lyu, Z. and Martins, J. R. R. A. (2015). Aerodynamic Shape Optimization of an Adaptive Morphing Trailing-Edge Wing. *Journal of Aircraft*, 52(6), 1951–1970. ISSN 0021-8669. doi:10.2514/1.C033116.

[3] Ghaffarian, S., Field, M., Reynolds, K., et al. (2013). Elastically Shaped Wing Optimization and Aircraft Concept for Improved Cruise Efficiency, 1–44. doi:doi:10.2514/6.2013-141.

[4] Nguyen, N., Kaul, U., Lebofsky, S., et al. (2010). Development of Variable Camber Continuous Trailing Edge Flap for Performance Adaptive Aeroelastic Wing. doi: 10.4271/2015-01-2565.

[5] Nguyen, N. and Ting, E. (2014). Flutter analysis of mission-adaptive wing with Variable Camber Continuous Trailing Edge Flap. *55th AIAA/ASMe/ASCE/AHS/SC Structures, Structural Dynamics, and Materials Conference*, 1–39. doi:10.2514/6.2014-0839.

[6] Sr., J. U., Nguyen, N., Ippolito, C., et al. (2013). A Mission-Adaptive Variable Camber Flap Control System to Optimize High Lift and Cruise Lift-to-Drag Ratios of Future N + 3 Transport Aircraft. *51st AIAA Aerospace Sciences Meeting including the New Horizons Forum and Aerospace Exposition, 7-10 January, Grapevine*, 1–24. doi:10.2514/6.2013-214.

[7] Kota, S., Osborn, R., Ervin, G., et al. (2006). Mission Adaptive Compliant Wing Design , Fabrication and Flight Test Mission Adaptive Compliant Wing. *Rtompavt*, 1–19.

[8] Hetrick, J. A., Osborn, R. F., Kota, S., et al. (2007). Flight Testing of Mission Adaptive Compliant Wing. *48th AIAAASMEASCEAHSASC Structures Structural Dynamics and Materials SDM Conference*, 1–17. ISSN 02734508. doi:10.2514/6.2007-1709.

[9] Cramer, N. B., Cheung, K., and Swei, S. S.-M. (2016). Design and Testing of a Lattice-based Cellular Component Active Twist Wing. *24th AIAA/AHS Adaptive Structures Conference*, 1–11. doi:doi:10.2514/6.2016-1085.

[10] Jenett, B., Calisch, S., Cellucci, D., et al. (2016). Digital Morphing Wing: Active Wing Shaping Concept Using Composite Lattice-Based Cellular Structures. *Soft Robotics*, 4(1), soro.2016.0032. ISSN 2169-5172. doi:10.1089/soro.2016.0032.

[11] Su, W., Swei, S. S.-M., and Zhu, G. G. (2016). Optimum wing shape of highly flexible morphing aircraft for improved flight performance. *Journal of Aircraft*, 53(5), 1305–1316. doi:10.2514/1.C033490.

[12] Su, W. and Cesnik, C. E. S. (2010). Nonlinear aeroelasticity of a very flexible blended-wing-body aircraft. *Journal of Aircraft*, 47(5), 1539–1553. ISSN 0021-8669. doi: 10.2514/1.47317.

[13] Su, W. and Cesnik, C. E. S. (2011). Dynamic response of highly flexible flying wings. *AIAA Journal*, 49(2), 324–339. ISSN 0001-1452. doi:10.2514/1.J050496.

[14] Su, W. and Cesnik, C. E. S. (2014). Strain-based analysis for geometrically nonlinear beams: A modal approach. *Journal of Aircraft*, 51(3), 890–903. ISSN 0021-8669. doi: 10.2514/1.C032477.

[15] Su, W. and Cesnik, C. E. S. (2011). Strain-based geometrically nonlinear beam formulation for modeling very flexible aircraft. *International Journal of Solids and Structures*, 48(16-17), 2349–2360. ISSN 0020-7683. doi:10.1016/j.ijsolstr.2011.04.012.

[16] Palacios, R. and Cesnik, C. E. S. (2005). Cross-sectional analysis of nonhomogeneous anisotropic active slender structures. *AIAA Journal*, 43(12), 2624–2638. ISSN 0001-1452. doi:10.2514/1.12451.

[17] Shearer, C. M. and Cesnik, C. E. S. (2007). Nonlinear flight dynamics of very flexible aircraft. *Journal of Aircraft*, 44(5), 1528–1545. ISSN 0021-8669. doi:10.2514/1.27606.

[18] Peters, D. A. and Johnson, M. J. (1994). Finite-State Airloads for Deformable Airfoils on Fixed and Rotating Wings. *Proceedings of Symposium on Aeroelasticity anf Fluid Structure Interaction Problems ASME Winter Annual Meeting*, 1–28.

[19] Tang, D. and Ã, E. H. D. (2006). Experimental and theoretical study of gust response for a wing store model with freeplay. *Journal of Sound and Vibration*, 295(3), 659–684. doi:10.1016/j.jsv.2006.01.024.

COPYRIGHT STATEMENT